Nanoscale Advances

PAPER

View Article Online
View Journal | View Issue

Cite this: *Nanoscale Adv.*, 2024, **6**, 5092

Electrocatalytic activity of tungsten carbide hybrids with two different MOFs for water splitting: a comparative analysis

Umair Sohail, Erum Pervaiz,* Rafiq Khosa and Maryum Ali

Conventional energy resources are diminishing, and environmental pollution is constantly increasing because of the excessive use of fossil fuels to sustain the ever-increasing population and industrialization. This has raised concerns regarding a sustainable future. In the pursuit of addressing sustainability in industrial processes and energy systems, the production of green hydrogen is considered a promising and crucial solution to meet the growing energy demands. Water-splitting is one of the most effective technologies for producing clean and carbon-neutral hydrogen. Water-splitting is a scientifically emerging application, but it is commercially limited due to its economic non-viability. The sluggish kinetics and the high overpotential needed for the water-splitting reactions (HER and OER) have encouraged the scientific community to design electrocatalysts that address the concerns of low activity, efficiency and stability. Designing a hybrid catalyst using metal–organic frameworks (MOFs) with transition metal carbides can be a suitable approach to address the deficiencies of conventional water-splitting catalysts. In this study, we have designed and fabricated an electrocatalyst of tungsten carbide (WC) with two different MOFs (Zr-based and Fe-based) and explored their electrocatalytic activity for hydrogen generation in an alkaline medium. It should be noted that hybrids of tungsten carbide with a zirconia MOF (UiO-66) showed better electrocatalytic activity with low overpotentials of 104 mV (HER) and 152 mV (OER) at a current density of 10 mA cm^{-2}. This superior activity of WC with the Zr-MOF in comparison to the Fe-MOF is due to the synergistic effect of Zr present in UiO-66 grown on the WC matrix. Moreover, UiO-66 provides a larger electrocatalytic active surface area, so available active sites are more in UiO-66 as compared to the Fe-MOF. These findings set the stage for the systematic development and production of bi-functional hybrid catalysts with the potential to be utilized in water-splitting processes.

Received 5th April 2024
Accepted 20th July 2024

DOI: 10.1039/d4na00289j

rsc.li/nanoscale-advances

Introduction

The increasing worldwide population and associated excessive use of energy reserves has led to a drastic increase in environmental pollution and the diminution of their natural reservoirs, *i.e.*, fossil fuel, gas, and oil reservoirs.[1,2] Exploration of renewable and green energy technologies is the only option to tackle these problems for a sustainable future.[3–5] In this regard, hydrogen has attracted tremendous interest as a future fuel as it is green, clean, and renewable in nature with almost negligible environmental impact as it produces clean exhaust products.[6–8] At present, commercial hydrogen gas is produced mainly through methane reforming, hydrocarbon cracking, and coal gasification.[9,10] However, these techniques use fossil fuels as the raw material and result in the emission of greenhouse gases, which are extremely harmful to the environment.[11,12] Water-splitting is a carbon-neutral process for the production of hydrogen. During the water-splitting process, the water molecule is dissociated into hydrogen and oxygen.[13–15] The reactions for the process are slow and require a significant amount of energy input to proceed.[16] For the process to work in an energy-efficient manner, an effective catalyst is needed to speed up the kinetics of the reactions.[17] Until now, noble metal catalysts have been used because of their good stability and activity. For the hydrogen evolution reaction (HER) the best catalyst recorded is the Pt/C catalyst and for the oxygen evolution reaction, IrO_2/RuO_2 is the best catalyst observed. Because of their high cost, scarce reserves, and short lifespan, these catalysts are not economically viable. There is a need to find a cost-effective, nonpolluting, durable, abundantly available, and efficient catalyst for overall water-splitting.[18] Recent studies have explored numerous electrocatalysts for overall water splitting like noble metals Pd, Au, and Ru, heteroatom doped carbon, carbides, sulfides, nitrides, and transition metal oxides.[19] One of the effective methods employed is the formation of a hybrid

Heterogeneous Catalysis Lab, Department of Chemical Engineering, School of Chemical and Materials Engineering (SCME), National University of Sciences and Technology (NUST), Islamabad, 44000, Pakistan. E-mail: erum.pervaiz@scme.nust.edu.pk; Tel: +92 3324001027

catalyst with synergistic properties composed of different materials with different characteristics.[20] Synergistic properties are observed when two different nanomaterials are combined to create a hybrid or composite material. This means that the unique properties of both materials combine and enhance one another in the resulting hybrid material. For instance, when tungsten carbide is combined with UiO-66 in a hybrid, the conductive properties of WC and high porosity of UiO-66 combine and result in improved activity of the hybrid electrocatalysts owing to their individual properties.[21]

Recently, many nonnoble metal materials such as transition metal phosphides and sulfides, carbonaceous materials, MOFs, and transition metal-based catalysts have been widely explored for water-splitting reactions as a replacement for noble metal catalysts.[22–24] MOFs (UiO-66 and Prussian blue) have gained a lot of attention recently due to their unique crystal structure and excellent catalytic properties. Crystalline nature also influences the transfer of electrons in any catalyst. Therefore, MOFs have consistently emerged as suitable candidates due to the presence of metal as a central atom,[25,26] while tungsten carbides (WC and W_2C) possess unique catalytic activity for the HER similar to that of Pt catalysts.[27] Because of its superior electric conductivity, cost-effectiveness, and high corrosion resistance, WC can be considered a strong choice for electrocatalytic HER reactions.[28] However, pure WC shows strong adsorption for H, which translates to low activity for the HER in alkaline media.[29] A good approach to enhance the HER activity of tungsten carbide is to modify it by creating hybrids with MOFs.[30]

Prussian blue nanoparticles (PBNPs) are a metal–organic framework with Fe as a central atom connected to ligands. They have a substantial surface area along with active sites where hydrogen intermediates are adsorbed and converted to hydrogen molecules (H_2).[31] In PBNPs, the oxidation state of iron with nitrogen is +3, and with carbon, it is +2. Owing to this, electron transfer to the conduction band is very fast.[32–34] Additionally, PB complexes also exhibit good solubility, stability, porosity, low density, and flexible molecular structure.[35]

UiO-66 is a MOF with a Zr central atom with benzene-1,4-dicarboxylic acid as organic ligands. The crystal structure of UiO-66 is octahedral offering large surface area. The chemical, mechanical and electrical stabilities of UiO-66 are also quite high. Formation of high charge density and polarization takes place because of the strong bonding of the carboxylate O atom and Zr(IV) atom resulting in considerable activity for water-splitting.

Tao Zhao *et al.* prepared WC hybrids using two different temperatures and compared the electrocatalytic activity of both samples. In their paper, they reported that the WC hybrid prepared at 800 °C has a lower Tafel slope of 75 mV dec^{-1} than the one prepared at 600 °C (96.2 mV dec^{-1}). Overpotential also followed the same trend as that of the Tafel slope. The overpotential of the WC(800) was 375 mV, and that of the WC(600) was 495 mV at a current density of 20 mA cm^{-2} for the OER.[36] Jin Soo Kang *et al.* prepared nanoporous tungsten carbide. They reported that the overpotential of WC was 187.1 mV at 10 mA cm^{-2} with a Tafel slope of 87.8 mV dec^{-1}.[37] Lulu Qiao *et al.* reported the OER overpotential of nanohybrid WC to be 238 mV with a Tafel slope of 59 mV dec^{-1} and an HER overpotential of 98 mV at a current density of 10 mA cm^{-2} with a Tafel slope of 40 mV dec^{-1}.[38]

With the understanding from the literature that the catalytic activity of tungsten carbide will be enhanced with MOFs we synthesized hybrids of WC with PBNPs and UiO-66 MOFs and studied their electrochemical behavior. Pure tungsten carbide was synthesized by a solid–gas reaction while the hybrid of UiO-66 was prepared by a hydrothermal method and for PBNPs a sonication method was used. The electrochemical result shows that the hybrid performed better than the pure catalysts. The improved activity of the hybrids can be attributed to the structure modification, increased surface area, and the synergistic effects.

Experimental section

Materials

The chemicals and reagents used in this research, including ammonium metatungstate dihydrate (AMT), hydrochloric acid (HCl), polyvinylidene fluoride (PVDF) $(C_2H_2F_2)_n$, *N*-methyl-2-pyrrolidone (NMP) (C_5H_9NO), zirconium chloride ($ZrCl_2$), and dimethylformamide (DMF) (C_3H_7NO), were purchased from Sigma Aldrich. Acetic acid (CH_3COOH) and ethanol (C_2H_5OH) were from BDH. Fructose, potassium hexacyanoferrate trihydrate (PHCF) ($K_4[Fe(CN_6)\cdot 3H_2O]$), and terephthalic acid (BDC) ($C_8H_6O_4$) were from Merck. Activated carbon and deionized water were purchased from Science Center.

Synthesis of pure tungsten carbide (WC)

For the synthesis of tungsten carbide, a precursor was first prepared by using the hydrothermal method. The precursor was prepared by mixing 5 g of AMT and 4.6 g of fructose in deionized water. The mixture was poured into a hydrothermal reactor (*i.e.*, an autoclave with Teflon lining) and heated for 12 h at 220 °C. After reaction completion, the sample was washed thrice first with deionized water to remove extra ions and then with ethanol to remove unreacted reactants. It was then dried at 70 °C overnight. The precursor was then calcined using the solid–gas reaction in a tube furnace at 1050 °C for 2 h under an Ar/H_2 environment to obtain the final product. The flow rate of Ar/H_2 is 3/1 throughout the reaction.

Synthesis of pure Prussian blue nanoparticles (PBNPs)

For the synthesis of pure Prussian blue, 0.8 mg of potassium hexacyanoferrate trihydrate was mixed in 0.01 L of HCl solution. The solution was then sonicated for 480 minutes in an ultrasonication bath. After the completion of the reaction, the blue colour product obtained was separated and washed thrice first with deionized water to remove extra ions and then with ethanol to remove unreacted reactants. Then the product was dried at 40 °C overnight in a vacuum oven.

Synthesis of pure UiO-66

UiO-66 was synthesized using the solvothermal method. In this method, 0.15 g of zirconium chloride ($ZrCl_4$) and 0.115 g of

terephthalic acid (BDC) were mixed into 30 ml of dimethyl formamide (DMF) solvent. 2 ml of CH_3COOH (acetic acid) was added to the above solution. The mixture was mixed for 120 minutes, followed by 20 minutes of ultra-sonication. Then the solution was transferred to a 100 ml hydrothermal reactor and heated at 120 °C for 24 h. After the reaction was completed, the prepared product was washed with DMF and ethanol to remove extra ions and any non-reacted reactants. It was then dried at 70 °C overnight in the oven to obtain the final powder.

Synthesis of WC and Prussian blue hybrids

Hybrids were prepared using an *in situ* technique in which Prussian blue nanoparticles are grown on WC. Three hybrids were synthesized with different ratios of WC and potassium hexacyanoferrate trihydrate. The hybrid with an equal ratio of WC and PHCF (1 : 1) is termed WC1, the hybrid with a ratio of WC to PHCF of 2 : 1 is termed WC2, and the hybrid with a ratio of WC to PHCF of 1 : 2 is termed WC3. All the hybrids were prepared using the same procedure with varying quantities of WC and PHCF. In the typical synthesis of hybrid WC1, 2 mmol of WC was dispersed in 100 ml of HCl solvent (0.1 M), and 2 mmol of PHCF was introduced and sonicated for 8 h in the ultra-sonication bath. After 8 h, the product was washed thrice, first with deionized water, and dried at 40 °C overnight. For WC2, 4 mmol of WC was used, and in WC3, 4 mmol of PHCF was used; the rest of the procedure was the same as that of WC1.

Synthesis of WC and UIO-66 hybrids

Hybrids of WC with UiO-66 were synthesized using the hydrothermal method. In hybrid WC4, WC/UiO-66 is in a ratio of 1 : 1, WC5 has a ratio of WC/UiO-66 equal to 2 : 1, and WC6 has a WC/UiO-66 ratio equal to 1 : 2. In the typical synthesis of WC4 equal amounts of WC and $ZrCl_4$ were mixed in 30 ml of DMF which already contains 115 g of BDC. 2 ml acetic acid was added in the solution and mixed for 2 h. After properly mixing, the solution was sonicated for 20 minutes. The mixture was moved to a stainless-steel autoclave lined with Teflon and heated at 120 °C for 24 h. After the reaction, the product formed was washed with DMF and ethanol several times and dried at 70 °C for 24 h in the oven. In WC5, the amount of WC is double that of $ZrCl_4$, and in WC6, the amount of $ZrCl_4$ is double that of the WC, and the rest of the procedure is the same as that of WC4.

Preparation of the electrode

To prepare the working electrode, catalyst ink was first prepared and then deposited on treated nickel foam. Nickel foam was treated, before the deposition, with HCl and ethanol. To prepare the catalyst ink 2.5 mg of PVDF, 5 mg of carbon black, and 42.5 mg of the prepared catalyst were mixed in 0.3 to 0.4 ml of NMP solvent and sonicated for 4 h in the ultra-sonication bath. After 4 h, the prepared ink was drop cast on nickel foam. After the deposition, the foam was dried at 80 °C overnight and pressed under 1 bar pressure before use.

Material characterization

To study the nature of the material X-ray diffraction (XRD) was employed. This XRD was used for the compositional analysis, phase formation, and to determine the crystallinity of the prepared catalyst. Cu Kα radiation was employed in the process with 2θ values in the range of 0 to 90°. For the morphological study and elemental analysis of the prepared catalysts scanning electron microscopy (SEM) was used along with energy dispersive X-ray spectroscopy (EDX).

Electrochemical analysis

Origalys (model number 5) was used with a three-electrode assembly for the electrochemical study of the fabricated catalyst with a working electrode (prepared catalyst), the counter electrode (platinum wire), and the reference electrode (Ag/AgCl). The catalyst deposited on the nickel foam was the working electrode during the experimentation. 1 molar KOH solution was employed as the electrolyte. For ease in computations, the potential was converted to a reversible hydrogen electrode (RHE) scale using a mathematical equation (eqn (1)). The equation for the RHE used is as follows.

$$E_{RHE} = E_{Ag/AgCl} + 0.059 \times 14 + E^{\circ}_{Ag/AgCl} \quad (1)$$

In the given equation, pH is 14, and $E^{\circ}_{Ag/AgCl}$ is 0.1976.

Electrochemical characterization of the fabricated catalysts was done using electrochemical impedance spectroscopy (EIS) for resistances, linear sweep voltammetry (LSV) for the HER and OER, chronopotentiometry for stability and cyclic voltammetry (CV) for redox reactions. LSV was performed at a 10 mV s^{-1} scan rate with a potential range of 0 to $\pm$1.5 V. CV was performed at different scan rates with a potential range of 0 to 0.6 V. The Tafel slope was calculated using eqn (2).

$$\eta = c \log I + a \quad (2)$$

Here η is the overpotential, I is current, a is the Tafel constant, and c is the Tafel slope. On the X-axis the log of current density is plotted against potential on the Y-axis.

Turnover frequency was calculated using eqn (3).

$$\mathrm{TOF} = (j \times A)/(\alpha \times f \times n) \quad (3)$$

In the given equation, j is the current density, A is the surface area of the nickel foam on which the catalyst is deposited, f is the faradaic constant, n is the number of moles of the coated catalyst, and α is the number of electrons transferred which is 2 for the HER and 4 for the OER. EIS was performed at a voltage amplitude of 10 V and a frequency range of 0.1 Hz to 2 M Hz. To determine the stability of the catalyst, chronopotentiometry was performed for 24 h.

Results and discussion

Phase determination and crystal size

The X-ray diffraction technique was used to determine the phase, the crystal structure, and the crystal size of the prepared

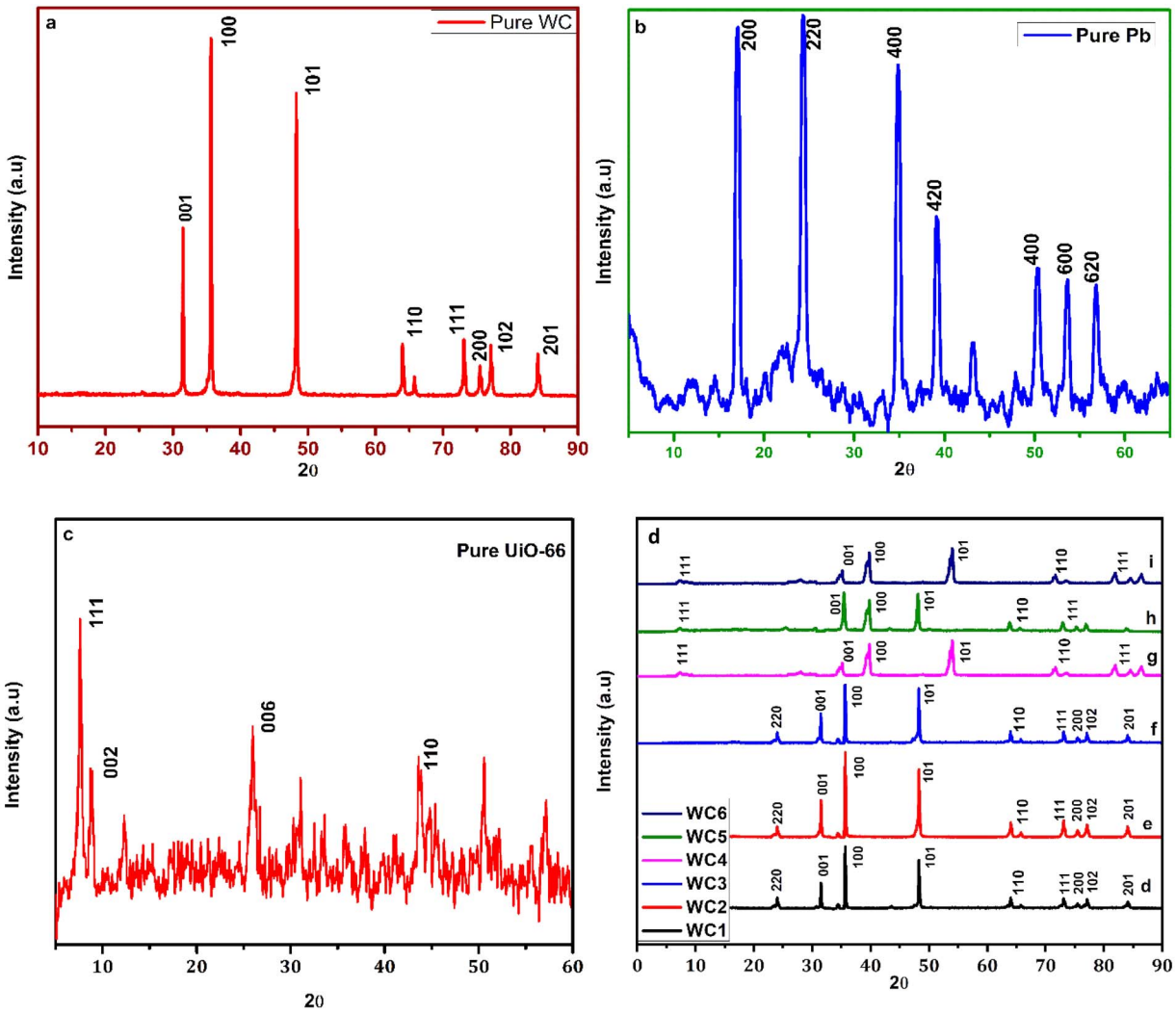

Fig. 1 XRD of the (a) pure WC, (b) pure PBNPs, (c) pure UiO-66, (d) (d) 1 : 1 WC/PHCF (WC1), (e) 2 : 1 WC/PHCF (WC2), (f) 1 : 2 WC/PHCF (WC3), (g) 1 : 1 WC/UiO-66 (WC4), (h) 2 : 1 WC/UiO-66 (WC5), and (i) 1 : 2 WC/UiO-66 (WC6).

catalyst. Fig. 1(a) shows the XRD pattern of pure tungsten carbide powder. These peaks are in agreement with the hexagonal crystal plane of WC (JCPDS 65-4539). The peaks appearing at 2θ angles of 31.3°, 35.7°, 48.2°, 64.1°, 65.4°, 73.1°, 75.6°, and 84.1° correspond to the planes of (001), (100), (101), (110), (111), (200), (102), and (201) respectively. XRD confirms the successful fabrication of hexagonal WC as given in the literature.[39] Fig. 1(b) is the XRD pattern of the prepared pure Prussian blue. This figure shows that peaks appeared for the planes of (200), (220), (400), (420), (422), (440), and (600) corresponding to 2θ values of 24.7°, 26.6°, 28.5°, 36.8°, 43.2°, 47.5°, and 51.3° respectively. These peaks are in accordance with JCPDS card number (73-0687), which confirmed the successful synthesis of pure PBNPs.[40] The XRD pattern of pure UiO-66 can be seen in Fig. 1(c). The figure shows the planes of (111), (002), (006), and (110) that are indexed to 2θ values of 7.4°, 8.4°, 26°, and 44.2°. The values agree with the values in the literature, confirming the formation of UiO-66. Fig. 1(d)–(i) show the XRD pattern of the prepared hybrids, *i.e.*, WC1, WC2, WC3, WC4, WC5, and WC6. In all the hybrids of WC with PBNPs, peaks are observed at 2θ angles of 24.8°, 31.5°, 35.6°, 48.2°, 64.1°, 65.4°, 73.1°, 75.6°, and 84.1° corresponding to the planes of (200), (001), (100), (101), (110), (111), (200), (102), and (201) respectively. The presence of (200) planes is confirmed by the characteristic peak of PBNPs at a 2θ angle of 24.8° in all the samples, while the peaks at 35.6, 48.2, and 64.1 are the distinctive peaks of WC which verify the synthesis of our hybrid. Moreover, from these peaks, we can also conclude that no change in the crystal structure occurs in WC after the modification with PBNPs. The slight shift in the characteristics peak of WC near 35° in all the hybrids compared to the pure WC is due to the slight increase in crystal size. Compared to the hybrids of PBNPs, there is a large shift in all the peaks of UiO-66 hybrids, *i.e.*, WC4 to WC6, toward the right. This shift indicates a decrease in the crystal structure and results in a larger surface area. In WC4 to WC6, prominent peaks appeared at 2θ values of 34°, 37.1°, 53.1°, and 73.2°, corresponding to the planes of (001), (100), (101), and (110), respectively. Meanwhile, in hybrid WC5 a shift can be seen only

Table 1 The prepared samples' crystal size, peak position, and FWHM

Electrocatalyst	Peak position (2θ)	FWHM (radian)	Crystal size (nm)	Average crystallite size (Å)
Pure WC	31.492, 35.634, 48.264, 63.993, 73.068	0.146, 0.182, 0.182, 0.109, 0.178	598, 480, 500, 927, 582	617.4
Pure PBNPs	17.5, 24.35, 34.8, 39.22, 50.33, 53.9	0.14, 0.189, 0.189, 0.189, 0.582, 0.287	574, 430, 411, 446, 151, 310	387.0
WC1	31.492, 35.643, 48.264, 63.993, 73.068, 30.663, 34.826	0.182, 0.182, 0.255, 0.109, 0.146, 0.218, 0.218	474, 480, 352, 927, 716, 392, 396	533.85
WC2	31.513, 35.434, 48.264, 64.011, 73.068, 65.833, 84.055	0.146, 0.146, 0.146, 0.109, 0.109, 0.291, 0.133	598, 605, 631, 928, 979, 334, 856	704.428
WC3	31.486, 35.634, 48.264, 63.976, 73.068, 30.976, 43.376	0.146, 0.146, 0.218, 0.146, 0.109, 0.218, 0.437	598, 605, 415, 679, 979, 393, 199	552
WC4	7.34, 25.32, 31.24, 35.40, 48.08, 72.934	0.437, 0.583, 0.291, 0.291, 0.328, 0.328	186, 142, 291, 295, 272, 309	249.166
WC5	7.35, 25.32, 31.245, 35.407, 48.08, 72.934	0.437, 0.583, 0.157, 0.22, 0.22, 0.189	186, 142, 554, 393, 410, 546	371.8
WC6	7.5, 25.22, 31.24, 35.40, 48.08, 72.934	0.537, 0.553, 0.241, 0.251, 0.318, 0.318	182, 138, 291, 295, 265, 310	246.833

in the peak appearing at 35°; this is because WC is present in a higher ratio in this hybrid, so no shift occurs in other peaks and the XRD pattern is the same as that of pure WC peaks. The samples' average crystallite size was calculated using the Scherrer equation (eqn (4)) using X'Pert HighScore.[41]

$$L = (M\lambda)(\mathrm{FWHM})(\cos\theta_c) \quad (4)$$

In this equation, L is the size of the crystal, M is Scherrer's constant, and its value is 0.9 (shape factor), λ is the X-ray wavelength, and its value is 0.155(nm), FWHM is the full width at half maximum and θ_c is the Bragg angle.

The calculated average crystal sizes of pure WC, pure PBNPs, WC1, WC2, WC3, WC4, WC5, and WC6 are 617, 387, 533.85, 704.428, 552, 249.166, 371.8, and 246.833 Å respectively as given in Table 1.

Morphological study and energy dispersive X-ray spectroscopy (EDX)

Scanning electron microscopy was employed to study the geomorphology of the fabricated samples. Fig. 2(a) shows the SEM image of pure WC. The prepared pure WC has spherical shape cubes of non-uniform sizes. It was observed that WC particles combine to form clusters. Fig. 2(b) is the SEM image of pure UiO-66. The spheres of UiO-66 can be seen to be the same as those reported in the literature. Fig. 2(c) is the SEM image of pure PBNPs. The figure shows cubes of PBNPs with uniform size which corroborates with the literature.[42,43] Fig. 2 (d)–(f) are the SEM images of hybrids WC1, WC2, and WC3. The images depict the formation of shapeless particles as if individual compounds are mixed. The improper shapes can be attributed to the synthesis route used for preparing the hybrids. In WC1 and WC2, none of the compounds is dominant on the other, while in WC3, cubes of PBNPs can be seen with WC particles fused on the surface of the cubes. Due to the presence of cube-like structure formation of PBNPs, the surface area of this hybrid is enhanced and, as a result, gives better activity compared to WC1 and WC2. Fig. 2(g)–(i) are the SEM images of WC4, WC5, and WC6. In WC5, the percentage of WC is greater than that of UiO-66, so the WC particle completely suppresses the presence of UiO-66. But in WC4 and WC6 the amount of UIO-66 is equal or greater so we can clearly see spheres in their SEM images.

Energy dispersive X-ray spectroscopy (EDX) of the best-performing catalyst, *i.e.*, WC3, was carried out to confirm the presence of all key elements in the hybrid. The result confirms that hybrid WC3 is composed of tungsten (W), carbon (C), and iron (Fe). The atomic percentages of W, C, and Fe are 40.3, 2.6, and 57%, as shown in Fig. 2(j). EDX shows that all the components are present in the sample, further confirming the successful synthesis of the WC and PBNP hybrid. The W, C, and Fe weight percentages in the sample were 89, 8, and 2 percent. Iron and tungsten are very good conductors and owing to the synergy between them, the charge transfer ability of the hybrid is enhanced resulting in enhanced electrocatalytic performance. Fig. 2(k) shows the EDX of WC4 in which the percentage WC and Zr is given. The result shows that the hybrid is composed of W, C, Zr, and O with atomic weight percentages of 9.8, 67.9, 4.4, and 17.9%, respectively. And the weight percentages of all these elements are 54.5, 24.7, 12.1, and 8.7%.

Electrochemical study

Hydrogen evolution reaction. For the electrochemical study of pure WC, pure PBNPs, pure UiO-66, and their hybrids, a three-electrode assembly is used in a 1 molar KOH solution. Fig. 3(a and b) show the linear sweep voltammetry curves of the HER. It can be observed that the prepared hybrids have greater activity as compared to pure WC, pure PBNPs, and pure UiO-66. The HER overpotentials reported for pure WC, pure PBNPs, and pure UiO-66 are 245, 209, and 201 mV at 10 mA cm^{-2} current density. The hybrids WC1, WC2, WC3, WC4, WC5, and WC6 have overpotentials of 207, 178, 162, 144, 161, and 104 mV, respectively, at 10 mV cm^{-2} current density. Compared to other hybrids, WC6 shows the lowest overpotential of 104 mV

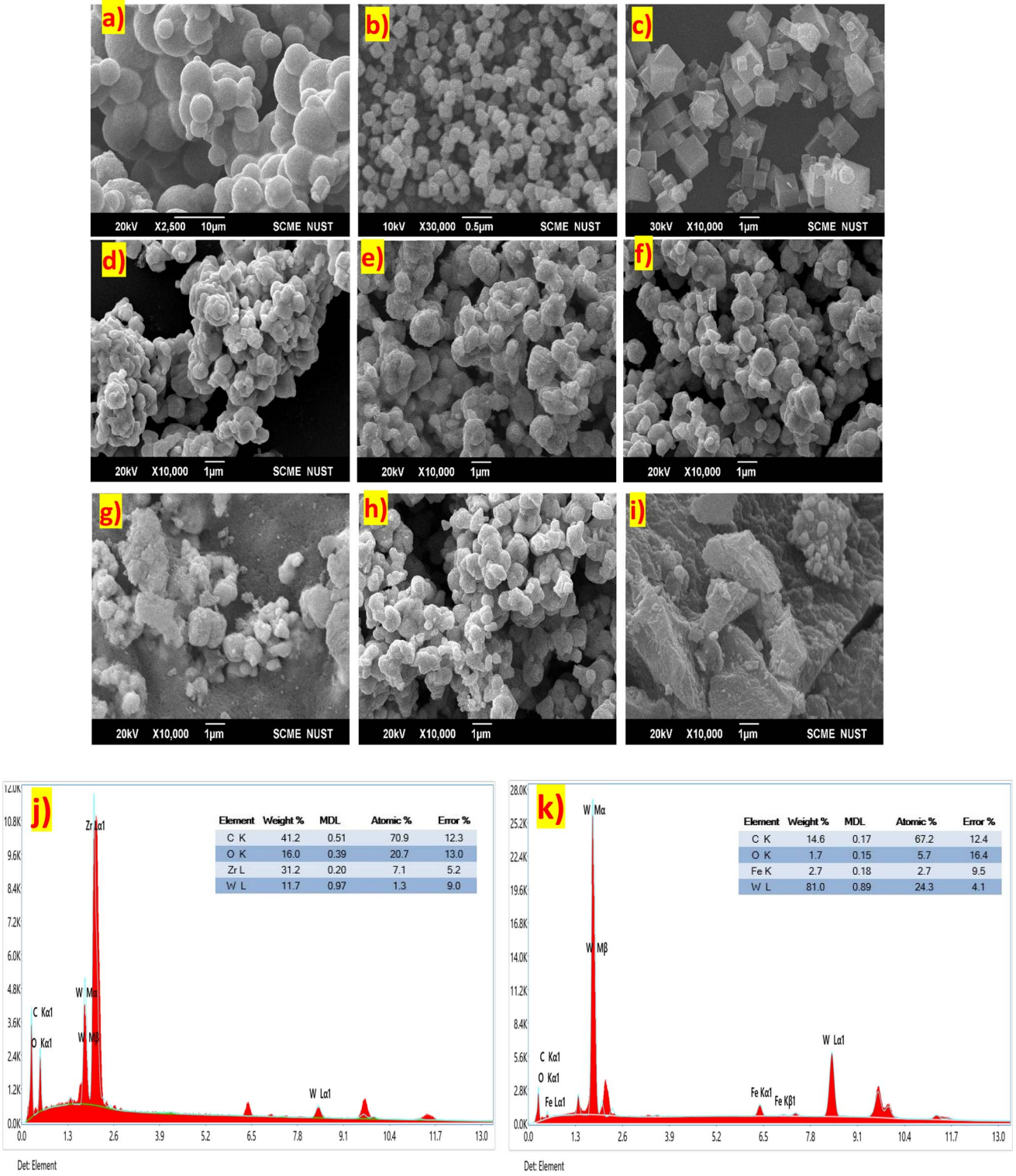

Fig. 2 (a–i) SEM images of all the prepared hybrids and pure samples; (j and k) EDX of WC4 and WC3.

representing good HER activity. Tungsten carbide is one of the best-conducting materials, so electron charge transfer occurs easily and gives us a low overpotential. Moreover, WC, Zr, and Fe are all materials that can be active sites for hydrogen evolution reactions. In the structure of PBNPs, there are two oxidation states of iron, *i.e.*, Fe^{2+} and Fe^{3+}. With carbon, the oxidation state of iron is +2, and with nitrogen, the +3 oxidation state is present. The oxidation state of W is +4 with carbon in WC. The oxidation state of Zr is also +4 with oxygen in UiO-66. Because of the greater number of active sites in Prussian blue

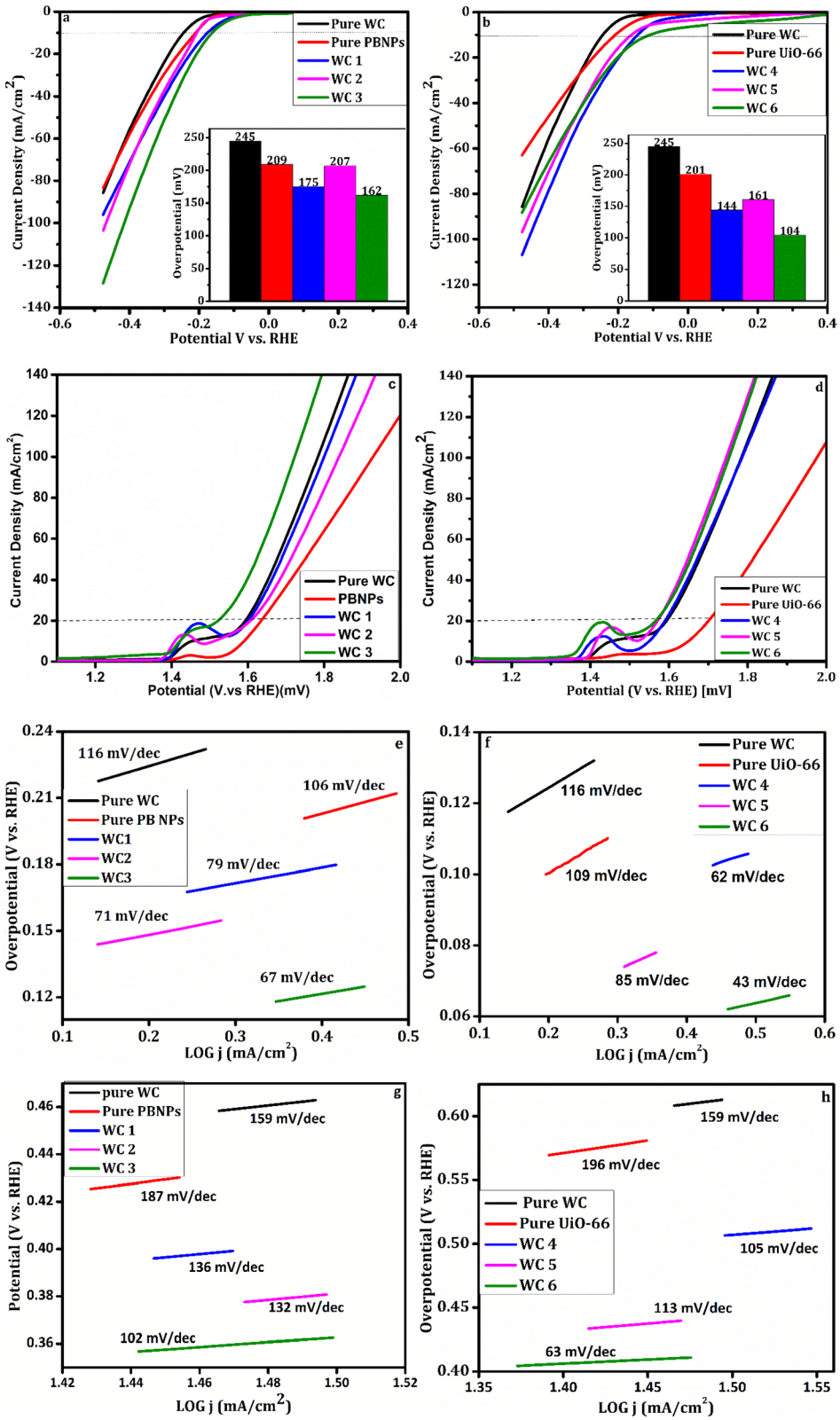

Fig. 3 (a and b) LSV curves for the HER, (c and d) LSV curves for the OER. (e and f) Tafel plots of the HER, (g and h) Tafel plots of the OER.

and UiO-66 compared to WC, the electron transfer due to these compounds is faster than electron transfer in pure WC. This results in excessive reduction of H^+ ions to H_2. Therefore, the HER activity of PBNPs and UiO-66 hybrids is higher than that of WC, as shown in Fig. 3(b). The increased HER activity is ascribed to the increased number of active sites in the hybrids

Table 2 Comparison of some catalysts in the literature with that in this work

Catalyst	Reaction type	Electrolyte	Tafel slope (mV dec^{-1})	Overpotential (mV)	Current density (mA cm^{-2})	Ref.
WC@UiO66	HER	1 M KOH	43	104	10	This work
	OER	1 M KOH	63	152	20	
W_2N/WC	HER	1 M KOH	47.4	148.5	10	45
	OER	1 M KOH	94	320		
WC*x*/C	HER	0.5 M H_2SO_4	85	264	10	46
W_2C-HS	HER	0.5 M H_2SO_4	67.8	153	10	47
WC with nickel doping	OER	1 M KOH	93	378	10	48
Co/W–C@NCNSs	OER	1 M KOH	75.5	323	10	49
W_6Co_6C@NC	OER	1 M KOH	54	286	10	50

(WC@UiO-66) and compact heterojunctions between WC and UiO-66. An effective edge site on the surface of the UiO-66 and WC is formed which limits charge carrier recombination and enhances charge migration, ensuring better electrocatalytic H_2 production. Further, the activity of the hybrids of UiO-66 is greater than that of the hybrids of PBNPs because of the larger surface area of the Zr MOF and its porous nature compared to the Fe MOF. So, the exposed active sites are more in the UiO-66, which results in rapid electron transfer and gives us a low overpotential of 104 mV.

To further study the catalytic activity of the prepared hybrids the Tafel slope was computed using eqn (2).[43] The Tafel slope correlates overpotential with reaction rate. In general, the Tafel slope is inversely proportional to the activity of a catalyst. The lower the Tafel slope of a catalyst, the better the activity of that electrocatalyst. The mechanism of the HER can be determined using the Tafel slope as it reveals the rate-limiting step of the HER. A smaller Tafel slope means high electron transport which translates to high catalyst activity with a low overpotential. The Tafel slope of the fabricated catalyst for the HER is given in Fig. 3(e and f). The figure shows that pure WC has the highest Tafel slope, and hybrid WC6 has the lowest Tafel slope amongst all the prepared samples, *i.e.*, 43 mV dec^{-1}. The Tafel slopes of pure WC, pure PBNPs, pure UiO-66, WC1, WC2, WC3, WC4, and WC5 are 116, 106, 109, 79, 71, 67, 62 and 85 mV dec^{-1} respectively. These values of the Tafel slope confirm that hybrid WC6 gives the highest activity, and pure WC shows the lowest activity among the prepared set of catalysts. The Tafel slope value of WC6, *i.e.*, 43 mV dec^{-1}, lies in the region of the Volmer–Heyrovsky mechanism.[44] The overall kinetics of the reactions are given as

Volmer step:

$$H_2O + E + e^- \rightarrow OH^- + E\text{–}H$$

Heyrovsky step:

$$H_2O + E + -H_{ads} + e^- \rightarrow OH^- + H_2$$

In the above equations, E is our working electrode which works as an adsorption site for water molecules. The water molecule in the KOH solution separates on the surface of the working electrode into adsorbed hydrogen and free hydroxyl ions in the Volmer step. This adsorbed hydrogen interacts with more molecules of water and is converted to a hydrogen molecule (H_2) and another hydroxyl ion (OH^-) in the Heyrovsky step. From the literature, it was gathered that the dissociation of water in the Volmer step can be enhanced by using WC and its hybrids with various MOFs. This is because of the conductive nature of WC and large surface area, and porous nature of MOFs. Supporting this literature study, our prepared hybrids of WC with PBNPs, *i.e.* WC3, and with UiO-66, *i.e.* WC6, both show outstanding results because of the synergistic effects of both substances in the hybrids.

Oxygen evolution reaction. The performance of the OER of the prepared hybrids was also observed using linear sweep voltammetry in 1 molar KOH (alkaline) electrolyte. In the OER, a four-electron transfer mechanism occurs instead of the two-electron transfer mechanism. Among the prepared samples the WC6 hybrid shows the lowest overpotential of 152 mV at 20 mA cm^{-2} current density in 1 M alkaline electrolyte. The other prepared hybrids, *i.e.* WC1, WC2, WC3, WC4, WC5, pure WC, pure UIO-66, and pure PBNPs, required overpotentials of 192, 190, 178, 173, 185, 172, 350, and 360 mV respectively to attain a 20 mA cm^{-2} current density in the same electrolyte solution as shown in Fig. 3(c and d). The peaks at 1.4 mV potential are due to the oxidation of the nickel foam in all the samples. So, these peaks do not show the activity of our catalyst and neither do they account for the splitting of water. These peaks appear at 10–15 mA cm^{-2} current density. Hence, we take the activity at 20 mA cm^{-2} current density for uniform results. WC6 shows the best activity among all the catalysts because of the presence of UiO-66, which has high stability, is highly porous, and has a higher surface area than that of PBNPs and WC. Although Fig. 3(c) indicates that the OER performance of the hybrid WC2 is inferior to that of pure WC based just on the overpotential, it is essential to take into account other parameters for a thorough assessment. Metrics such as the Tafel slope, current density, stability, turnover frequency, and electrochemical surface area are important factors in establishing the overall effectiveness of a catalyst. Moreover, the enhanced catalytic activity of all the hybrids as compared to the pure compounds is also because of the synergistic effects of both the compounds in the hybrids.

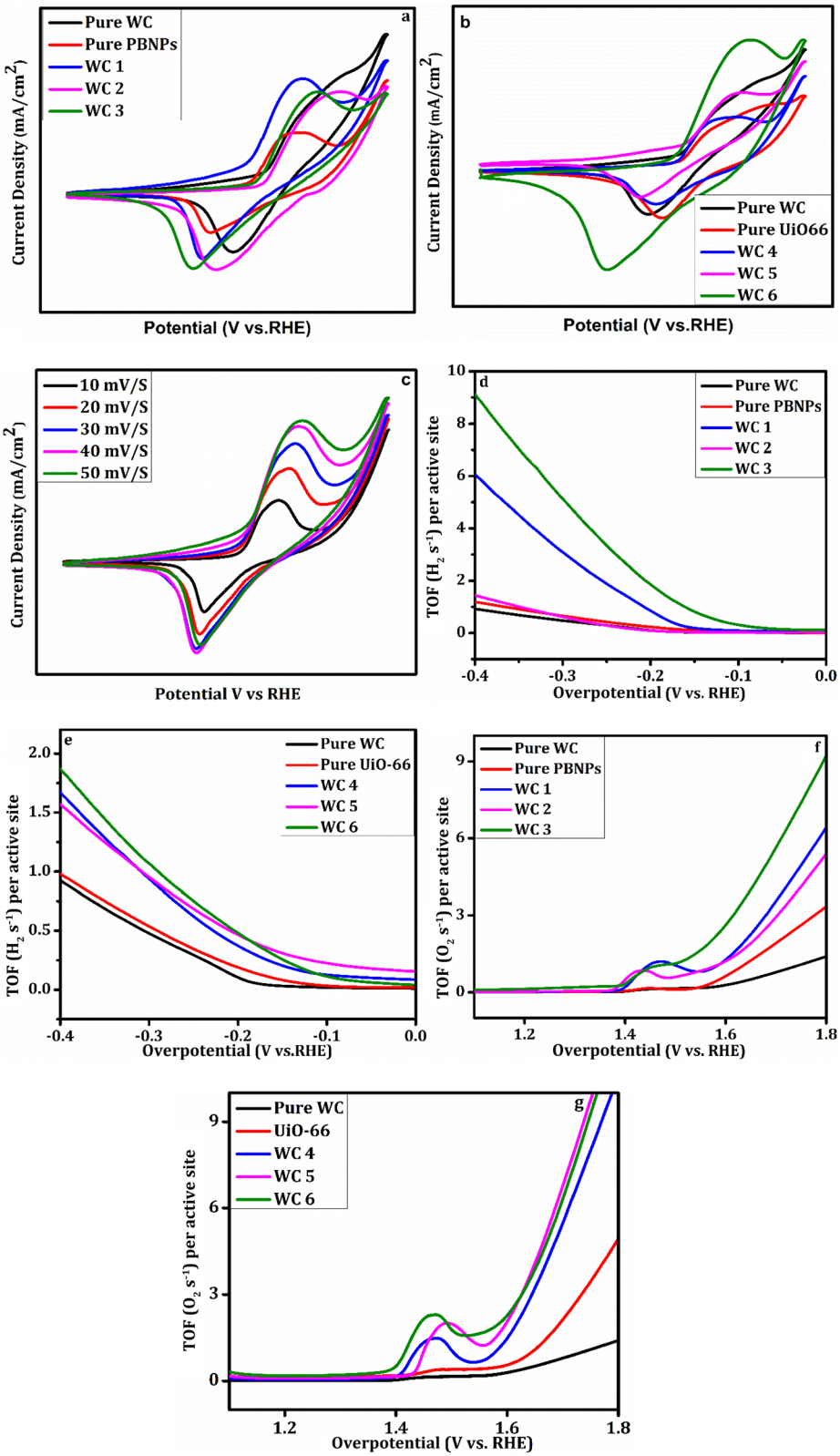

Fig. 4 (a) CVs of WC@PBNP hybrids, (b) CVs of WC@UiO-66 hybrids, (c) CV curves of WC6 at different scan rates, (d and e) TOF of the hybrids for the HER, (f and g) TOF of hybrids for the OER.

The overall properties of the hybrids are enhanced, and, as a result, the catalytic activity is also improved.

The Tafel plots for the OER of all the prepared samples are given in Fig. 3(g and h). It can be observed that WC6 has the smallest Tafel slope of 63 mV dec^{-1}. This low Tafel slope indicates that WC6 has a fast oxygen evolution charge transfer ability with enhanced reaction kinetics for electrocatalytic OER. This statement is verified by EIS. The Tafel slopes of all other hybrids, *i.e.*, pure WC, pure PBNPs, pure UiO-66, WC1, WC2, WC3, WC4, and WC5, are 159, 187, 196, 136, 132, 102, 105, and 113 mV dec^{-1} respectively. The Tafel slope of pure WC suggests that the hydroxyl ion's adsorption rate on the catalyst's surface is poor. Still, with the addition of PBNPs and UiO-66, the OER activity is enhanced, giving us low Tafel slope values. This phenomenon is due to oxygen absorption by transition metal cation sites. In the hybrid, the heterostructure of Fe, W, and Zr speeds up the electron transport, and as a result, electrochemical performance is improved compared to that of pure compounds. The overpotential of certain hybrids is presented in Table 2 to compare the values reported in the literature with the findings of this paper.

Cyclic voltammetry. To study the correlation between current density over a range of voltages (0 to 600 mV), cyclic voltammetry of all the fabricated catalysts was performed at a scan rate of 100 mV s^{-1}, as shown in Fig. 4(a and b). The graph of CV gives information about the thermodynamics of the oxidation and reduction reactions and the mechanism of the movement of the electron. Two distinct redox peaks are observed in the CV graph corresponding to the oxidation peak above and the reduction peak below.[51] From the CV of a catalyst, we can find the area under the curve, and the electrochemically active surface area (ESCA) is determined from that. Fig. 4(c) shows the CV graph of WC6 at different scan rates from 0 to 50 mV s^{-1}. In the given potential range, two redox peaks are shown. Transfer of charge occurs between the redox sites through WC6, and ions are transferred through the electrode's pores with no change in the structure. The CV profile of WC6 stays consistent with a steady increase in the area with the increase in the scan rate, which shows strong cyclic stability, better electrocatalytic efficiency, and low catalyst resistance. Increasing the scan rate decreases the absorption layer's impedance, resulting in a high current density. As the scan rate increases, the redox peaks increase gradually, indicating that the redox action is confined to the surface of WC6 and proving the stability of the catalyst. Yet another notable parameter to study the intrinsic activity of a catalyst is turnover frequency (TOF). TOF is the reactant exhausted or product established in a unit of time for the given catalyst. TOF was calculated using eqn (3). The TOF of WC6 observed at 0.4 V is 1.8 H_2 per s for the HER and 8 O_2 per s for the OER at 1.7 V, as seen in Fig. 4(d–g). This catalyst's excellent production ability is because of this hybrid's structural and electrocatalytic ability. The transfer of electrons is higher, resulting in more hydrogen and oxygen being produced compared to other hybrids.

Electrochemical impedance spectroscopy and chronopotentiometry. Another important parameter to determine the catalytic activity of electrocatalysts is electrochemical impedance spectroscopy (EIS). The EIS of all the prepared catalysts and the analog circuit are shown in Fig. 5(a, b and d). The test was performed in a frequency range of 200 kHz to 0.001 kHz in 1 molar alkaline electrolyte. In the Nyquist plot, imaginary impedance is given on the *y*-axis, and real impedance is given on the *x*-axis. EIS is used to find the charge transfer resistance R_{ct}, polarization resistance R_p, Warburg resistance W (resistance due to the electrode to electrolyte interface), and faradaic capacitance C_p. The resistance values are given in Table 3. Generally, insignificant values of R_{ct} have fast charge transfer ability.[52] Our best-performing catalyst, *i.e.* WC6, has a small semicircle compared to other catalysts, indicating that this catalyst offers low charge transfer resistance and hence shows good electrocatalytic activity verified from its Tafel slope values. Values of charge transfer resistance and solution resistance are noted in Table 3. One effective approach for finding a catalyst's electrocatalytic performance is to determine the electrochemically active surface area (ECSA). The performance of a catalyst is directly proportional to ECSA. The larger the electrochemically active surface area of the catalyst, the better the performance of that catalyst. The ECSA of the catalyst can be determined using eqn (5).[53]

$$\mathrm{ECSA} = C_p/C_s \tag{5}$$

In the above equation, the specific capacitance value is constant and given as 40 μF cm^{-2}. C_p is the electrochemical capacitance, and it is equal to

$$C_p = A/(2 \times m \times k)(V_2 - V_1) \tag{6}$$

Here A is the area under the CV curve, determined from the CV curve through the Origin software. m is the mass loaded. k is the scan rate at which the experiment is performed here; it is 0.05 V s^{-1}. $V_2 - V_1$ gives the difference between the final and initial potential; its value is 0.6 V.

The ECSA of all prepared catalysts is given in Table 3.

For practical applications, the stability or durability of the catalyst is an important parameter. It can be examined using chronopotentiometry to find the changes in the overpotential current density with time. The stability test of WC6 is performed for 20 h to get a chronopotentiometry curve in 1 molar KOH electrolyte solution. Fig. 5(c) shows that the catalyst has good stability with a very small drop in activity as time passes. This stability is because of the structural properties of the catalyst. Fig. 5(e) depicts the chronoamperometry of WC6, and it shows that the prepared catalyst is stable for 20 h maintaining a constant potential. Fig. 5(f and g) show the activity of the HER and OER before and after the stability test and they show that there is a slight decrease in the activity of the catalyst after 20 h as can be confirmed from chronopotentiometry.

Proposed mechanism

For the HER, the proposed mechanism will be that of Volmer–Heyrovsky. This can be found from the Tafel slope values. In the first step, an intermediate of H* is formed from the adsorbed

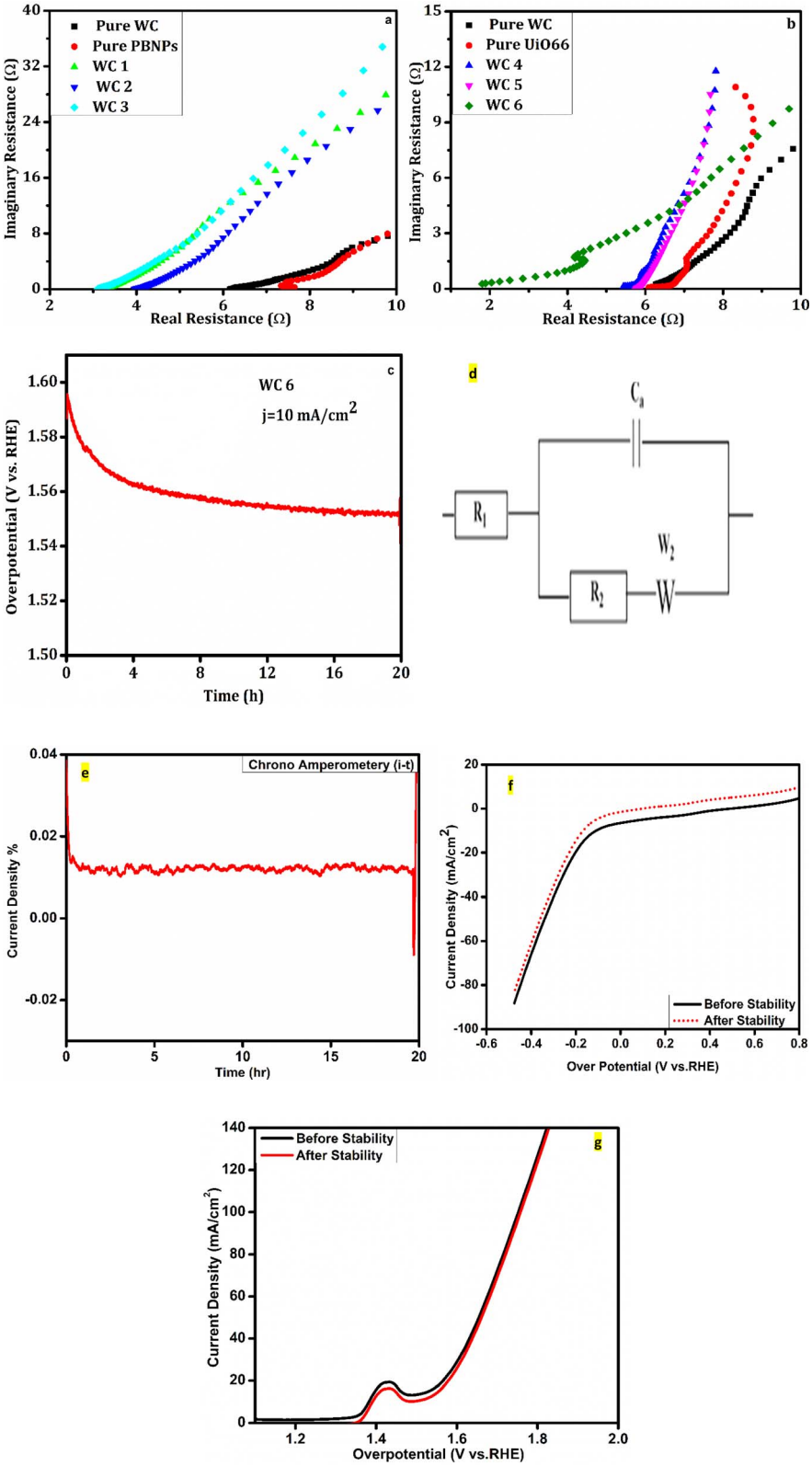

Fig. 5 (a and b) EIS of the prepared samples, (c) chronopotentiometry of WC6, (d) analogue circuit, (e) *i*–*t* test of WC6, (f and g) HER and OER after the stability test.

Table 3 Resistance and ECSA of the prepared samples

Catalyst	R_s	R_{ct}	ECSA
WC	6.1878	2.4108	2170
PBNPs	7.6218	3.8167	1828
UiO-66	5.996	1.9296	2188.36
WC1	6.2753	1.7712	2694
WC2	3.264	1.5214	2458.333
WC3	5.778	1.03	3504.312
WC4	3.107	0.898	3288.061
WC5	2.1558	0.289	3111.37
WC6	1.81	0.257	6431.719

hydrogen on the electrode surface. In the second step, a molecule of hydrogen is formed from the electrochemical desorption of hydrogen generated in the first step. The overall mechanism with the corresponding reactions are given as

1. Volmer reaction

$$H_2O + e^- \rightarrow H^* + OH^-$$

2. Heyrovsky reaction

$$H_2O + e^- + H^* \rightarrow H_2 + OH^-$$

For the OER, a four-step mechanism is used, as shown in these equations; the reactions that are taking place are given as

$$E + OH^- \rightarrow EOH + e^-$$

$$EOH + OH^- \rightarrow EO + H_2O + e^-$$

$$EO + OH^- \rightarrow EOOH + e^-$$

$$EOOH + OH^- \rightarrow E + O_2 + H_2O + e^-$$

In these equations, E is our catalyst where hydroxyl ions combine and convert into EOH in the first step with the removal of an electron. In the 2nd step, the catalyst is reduced to E–O in the presence of another OH^- ion with the production of a water molecule. In the third step, the oxidized catalyst can take two paths: either be directly reduced to E with the release of half molecule of oxygen or combine with another molecule of OH^- and convert to EOOH. In the final step, the OH^- ion reacts with the catalyst and reduces it to E and a water molecule along with an oxygen molecule is produced.

Conclusion and future prospects

To summarize, a comparison of WC hybrids with two different MOFs has been made for overall water splitting. Spherical WC particles, cubic PBNPs, octahedral UiO-66, and their hybrids are fabricated through solid–gas, sonication, and hydrothermal techniques. Among the optimized hybrids, *i.e.*, WC3 and WC6, the hybrid of PBNPs and UiO-66 with WC, respectively shows better activity than pure compounds for overall water splitting. For WC6, low overpotentials of 104 mV and 152 mV are noticed for the HER and OER in 1 molar alkaline KOH at 10 mA cm^{-2} and 20 mA cm^{-2} current density, respectively. This shows that the overall performance of water splitting is increased as this catalyst provides a low overpotential for both the HER and OER at the same time. This exceptional activity of WC6 is because of the synergistic effects of the materials present in the hybrid. WC6 shows better activity than WC3 because UiO-66 has a large surface area and is porous, which gives more active sites for hydrogen absorbance than PBNPs; as a result, electron transfer takes place rapidly. These findings set the stage for the systematic development and production of bi-functional hybrid catalysts with the potential to be utilized in water-splitting processes. Nevertheless, deeper understanding of molecular-level process kinetics, the structure–catalysis link, and interface electron transport is necessary to develop more effective catalysts.

Data availability

Data will be made available by the authors on request.

Author contributions

Umair Sohail: performing experiments, plotting the results and writing the paper. Erum Pervaiz: proof reading and supervision of experiments and providing funding. Rafiq Khosa: plotting the results and proof reading. Maryum Ali: supervision of the experiments and plotting the results.

Conflicts of interest

The authors declare that they have no known competing financial interests or personal relationships that could have appeared to influence the work reported in this paper.

Acknowledgements

Erum Pervaiz would like to acknowledge HEC Pakistan for grant 2017/HEC/NRPU/10482. This work was supported by the School of Chemical and Materials Engineering (SCME), National University of Science and Technology, Islamabad, Pakistan.

References

1 U. Sohail, E. Pervaiz, M. Ali, R. Khosa, A. Shakoor and U. Abdullah, Role of tungsten carbide (WC) and its hybrids in electrochemical water splitting application-a comprehensive review, *FlatChem*, 2022, **35**, 100404.
2 R. Moliner, M. J. Lázaro and I. Suelves, Analysis of the strategies for bridging the gap towards the hydrogen economy, *Int. J. Hydrogen Energy*, 2016, **41**(43), 19500–19508.
3 A. M. Abdalla, S. Hossain, O. B. Nisfindy, A. T. Azad, M. Dawood and A. K. Azad, Hydrogen production, storage, transportation and key challenges with applications: a review, *Energy Convers. Manage.*, 2018, **165**, 602–627.
4 U. Abdullah, M. Ali, E. Pervaiz and R. Khosa, An inclusive perspective on the recent development of tungsten-based

catalysts for overall water-splitting: a review, *Int. J. Energy Res.*, 2022, **46**(8), 10228–10258.
5 J. Sun, P. Leng, Y. Xie, X. Yu, K. Qu, L. Feng, *et al.*, Co single atoms and Co nanoparticle relay electrocatalyst for rechargeable zinc air batteries, *Appl. Catal., B*, 2022, **319**, 121905.
6 R. Khosa, E. Pervaiz, U. Abdullah, M. Ali, U. Sohail and A. Shakoor, An insight on molybdenum phosphide and its hybrids as catalyst for electrochemical water splitting: a mini-review, *Mol. Catal.*, 2022, **528**, 112514.
7 M. Amoretti, Towards a peer-to-peer hydrogen economy framework, *Int. J. Hydrogen Energy*, 2011, **36**(11), 6376–6386.
8 N. Gerloff, Environmental costs of green hydrogen production as energy storage for renewable energies, *MRS Energy Sustain.*, 2023, **10**(2), 174–180.
9 M. Ni, M. K. H. Leung, D. Y. C. Leung and K. Sumathy, A review and recent developments in photocatalytic water-splitting using TiO_2 for hydrogen production, *Renewable Sustainable Energy Rev.*, 2007, **11**(3), 401–425.
10 P. Vaghela, V. Pandey, A. Sircar, K. Yadav, N. Bist and R. Kumari, Energy storage techniques, applications, and recent trends: a sustainable solution for power storage, *MRS Energy Sustain.*, 2023, **10**(2), 261–276.
11 R. Zahra, E. Pervaiz, M. Yang, O. Rabi, Z. Saleem, M. Ali, *et al.*, A review on nickel cobalt sulphide and their hybrids: Earth abundant, pH stable electro-catalyst for hydrogen evolution reaction, *Int. J. Hydrogen Energy*, 2020, **45**(46), 24518–24543.
12 A. Khan, I. Ali, W. Farooq, S. R. Naqvi, M. T. Mehran, A. Shahid, *et al.*, Investigation of combustion performance of tannery sewage sludge using thermokinetic analysis and prediction by artificial neural network, *Case Stud. Therm. Eng.*, 2022, **40**, 102586.
13 Y. Cao, L. Shen, X. Hu, Z. Du and L. Jiang, Low temperature desulfurization on Co-doped α-FeOOH: tailoring the phase composition and creating the defects, *Chem. Eng. J.*, 2016, **306**, 124–130.
14 Y. Choquette, L. Brossard, A. Lasia and H. Menard, Study of the kinetics of hydrogen evolution reaction on Raney nickel composite-coated electrode by AC impedance technique, *J. Electrochem. Soc.*, 1990, **137**(6), 1723.
15 A. Lasia and A. Rami, Kinetics of hydrogen evolution on nickel electrodes, *J. Electroanal. Chem. Interfacial Electrochem.*, 1990, **294**(1–2), 123–141.
16 K. Maeda, Photocatalytic water splitting using semiconductor particles: history and recent developments, *J. Photochem. Photobiol., C*, 2011, **12**(4), 237–268.
17 M. Ali, E. Pervaiz, T. Noor, O. Rabi, R. Zahra and M. Yang, Recent advancements in MOF-based catalysts for applications in electrochemical and photoelectrochemical water splitting: a review, *Int. J. Energy Res.*, 2021, **45**(2), 1190–1226.
18 Y. Yan, B. Y. Xia, B. Zhao and X. Wang, A review on noble-metal-free bifunctional heterogeneous catalysts for overall electrochemical water splitting, *J. Mater. Chem. A*, 2016, **4**(45), 17587–17603.
19 C. Li, R. Xu, S. Ma, Y. Xie, K. Qu, H. Bao, *et al.*, Sulfur vacancies in ultrathin cobalt sulfide nanoflowers enable boosted electrocatalytic activity of nitrogen reduction reaction, *Chem. Eng. J.*, 2021, **415**, 129018.
20 S. H. Jensen, P. H. Larsen and M. Mogensen, Hydrogen and synthetic fuel production from renewable energy sources, *Int. J. Hydrogen Energy*, 2007, **32**(15), 3253–3257.
21 T. E. Agustina, H. M. Ang and V. K. Vareek, A review of synergistic effect of photocatalysis and ozonation on wastewater treatment, *J. Photochem. Photobiol., C*, 2005, **6**(4), 264–273.
22 X. Zou and Y. Zhang, Noble metal-free hydrogen evolution catalysts for water splitting, *Chem. Soc. Rev.*, 2015, **44**(15), 5148–5180.
23 S. Chandrasekaran, L. Yao, L. Deng, C. Bowen, Y. Zhang, S. Chen, *et al.*, Recent advances in metal sulfides: from controlled fabrication to electrocatalytic, photocatalytic and photoelectrochemical water splitting and beyond, *Chem. Soc. Rev.*, 2019, **48**(15), 4178–4280.
24 M. Ali and E. Pervaiz, Effect of synthesis route on electrocatalytic water-splitting activity of MoS_2/UiO-66 hybrid, *Mol. Catal.*, 2022, **519**, 112136.
25 B. Feng, H. Wang, D. Wang, H. Yu, Y. Chu and H.-T. Fang, Fabrication of mesoporous metal oxide coated-nanocarbon hybrid materials *via* a polyol-mediated self-assembly process, *Nanoscale*, 2014, **6**(23), 14371–14379.
26 L. Zeng, W. Zeng, Y. Jiang, X. Wei, W. Li, C. Yang, *et al.*, A flexible porous carbon nanofibers-selenium cathode with superior electrochemical performance for both Li-Se and Na-Se batteries, *Adv. Energy Mater.*, 2015, **5**(4), 1401377.
27 C. Liu, J. Zhou, Y. Xiao, L. Yang, D. Yang and D. Zhou, Structural and electrochemical studies of tungsten carbide/carbon composites for hydrogen evolution, *Int. J. Hydrogen Energy*, 2017, **42**(50), 29781–29790.
28 Y.-J. Ko, J.-M. Cho, I. Kim, D. S. Jeong, K.-S. Lee, J.-K. Park, *et al.*, Tungsten carbide nanowalls as electrocatalyst for hydrogen evolution reaction: new approach to durability issue, *Appl. Catal., B*, 2017, **203**, 684–691.
29 S. Sagadevan, I. Das, P. Singh and J. Podder, Synthesis of tungsten carbide nanoparticles by hydrothermal method and its characterization, *J. Mater. Sci.: Mater. Electron.*, 2017, **28**, 1136–1141.
30 X. Li, X. Hao, A. Abudula and G. Guan, Nanostructured catalysts for electrochemical water splitting: current state and prospects, *J. Mater. Chem. A*, 2016, **4**(31), 11973–12000.
31 H. Wu, Q. Liu, L. Zhang, Y. Tang, G. Wang and G. Mao, Novel nanostructured WO_3@Prussian blue heterojunction photoanodes for efficient photoelectrochemical water splitting, *ACS Appl. Energy Mater.*, 2021, **4**(11), 12508–12514.
32 M. Zhang, Y. Chen, J.-N. Chang, C. Jiang, W.-X. Ji, L.-Y. Li, *et al.*, Efficient charge migration in chemically-bonded Prussian blue analogue/CdS with beaded structure for photocatalytic H_2 evolution, *JACS Au*, 2021, **1**(2), 212–220.
33 A. Gotoh, H. Uchida, M. Ishizaki, T. Satoh, S. Kaga, S. Okamoto, *et al.*, Simple synthesis of three primary colour nanoparticle inks of Prussian blue and its analogues, *Nanotechnology*, 2007, **18**(34), 345609.

34 M. Ali, E. Pervaiz, U. Sikandar and Y. Khan, A review on the recent developments in zirconium and carbon-based catalysts for photoelectrochemical water-splitting, *Int. J. Hydrogen Energy*, 2021, **46**(35), 18257–18283.

35 Y. Feng, Q. Chen, M. Jiang and J. Yao, Tailoring the properties of UiO-66 through defect engineering: a review, *Ind. Eng. Chem. Res.*, 2019, **58**(38), 17646–17659.

36 T. Zhao, J. Gao, J. Wu, P. He, Y. Li and J. Yao, Highly active cobalt/tungsten carbide@N-doped porous carbon nanomaterials derived from metal-organic frameworks as bifunctional catalysts for overall water splitting, *Energy Technol.*, 2019, **7**(4), 1800969.

37 J. S. Kang, J. Kim, M. J. Lee, Y. J. Son, J. Jeong, D. Y. Chung, *et al.*, Electrochemical synthesis of nanoporous tungsten carbide and its application as electrocatalysts for photoelectrochemical cells, *Nanoscale*, 2017, **9**(17), 5413–5424.

38 L. Qiao, A. Zhu, W. Zeng, R. Dong, P. Tan, Z. Ding, *et al.*, Achieving electronic structure reconfiguration in metallic carbides for robust electrochemical water splitting, *J. Mater. Chem. A*, 2020, **8**(5), 2453–2462.

39 M. Zeng, Y. Chen, J. Li, H. Xue, R. G. Mendes, J. Liu, *et al.*, 2D WC single crystal embedded in graphene for enhancing hydrogen evolution reaction, *Nano Energy*, 2017, **33**, 356–362.

40 U. Abdullah, M. Ali and E. Pervaiz, Cadmium sulfide embedded Prussian blue as highly active bifunctional electrocatalyst for water-splitting process, *Int. J. Hydrogen Energy*, 2022, **47**(49), 21160–21172.

41 V. S. Vinila, R. Jacob, A. Mony, H. G. Nair, S. Issac, S. Rajan, *et al.*, XRD studies on nano crystalline ceramic superconductor PbSrCaCuO at different treating temperatures, *Cryst. Struct. Theory Appl.*, 2014, **2014**, 43963.

42 M. B. Zakaria, A. A. Belik, C. H. Liu, H. Y. Hsieh, Y. T. Liao, V. Malgras, *et al.*, Prussian blue derived nanoporous iron oxides as anticancer drug carriers for magnetic-guided chemotherapy, *Chem.–Asian J.*, 2015, **10**(7), 1457–1462.

43 R. Khan, M. T. Mehran, M. M. Baig, B. Sarfraz, S. R. Naqvi, M. B. K. Niazi, *et al.*, 3D hierarchical heterostructured LSTN@NiMn-layered double hydroxide as a bifunctional water splitting electrocatalyst for hydrogen production, *Fuel*, 2021, **285**, 119174.

44 R. Qiang, Y. Du, D. Chen, W. Ma, Y. Wang, P. Xu, *et al.*, Electromagnetic functionalized Co/C composites by *in situ* pyrolysis of metal-organic frameworks (ZIF-67), *J. Alloys Compd.*, 2016, **681**, 384–393.

45 J. Diao, Y. Qiu, S. Liu, W. Wang, K. Chen, H. Li, *et al.*, Interfacial engineering of W_2N/WC heterostructures derived from solid-state synthesis: a highly efficient trifunctional electrocatalyst for ORR, OER, and HER, *Adv. Mater.*, 2020, **32**(7), 1905679.

46 Z. Chen, M. Qin, P. Chen, B. Jia, Q. He and X. Qu, Tungsten carbide/carbon composite synthesized by combustion-carbothermal reduction method as electrocatalyst for hydrogen evolution reaction, *Int. J. Hydrogen Energy*, 2016, **41**(30), 13005–13013.

47 Y. Ling, F. Luo, Q. Zhang, K. Qu, L. Guo, H. Hu, *et al.*, Tungsten carbide hollow microspheres with robust and stable electrocatalytic activity toward hydrogen evolution reaction, *ACS Omega*, 2019, **4**(2), 4185–4191.

48 S. Lu, J. Wu, H. Hu, X. Pan, Z. Hu, H. Li, *et al.*, Boosting oxygen evolution through phase and electronic modulation of highly dispersed tungsten carbide with nickel doping, *J. Colloid Interface Sci.*, 2021, **585**, 258–266.

49 X. Ma, *Advanced Energy Efficiency Technologies for Solar Heating, Cooling and Power Generation*, Springer, 2019.

50 J. Chen, B. Ren, H. Cui and C. Wang, Constructing pure phase tungsten-based bimetallic carbide nanosheet as an efficient bifunctional electrocatalyst for overall water splitting, *Small*, 2020, **16**(23), 1907556.

51 J. Liang and D. W. Wang, Design rationale and device configuration of lithium-ion capacitors, *Adv. Energy Mater.*, 2022, **12**(25), 2200920.

52 L. Bu, X. Chen, Q. Song, D. Jiang, X. Shan, W. Wang, *et al.*, Supersensitive detection of chloramphenicol with an EIS method based on molecularly imprinted polypyrrole at UiO-66 and CDs modified electrode, *Microchem. J.*, 2022, **179**, 107459.

53 P. Connor, J. Schuch, B. Kaiser and W. Jaegermann, The determination of electrochemical active surface area and specific capacity revisited for the system MnO_x as an oxygen evolution catalyst, *Z. Phys. Chem.*, 2020, **234**(5), 979–994.